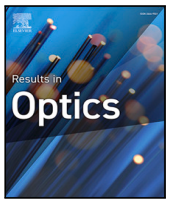
Results in Optics 24 (2026) 101121



Contents lists available at ScienceDirect

Results in Optics

journal homepage: www.elsevier.com/locate/rio



Calibration-oriented analysis of ITU-T grid alignment limits in athermal cyclic arrayed waveguide gratings

Jozef Chovan [a,*], Dana Seyringer [b], Anton Kuzma [a,c], Martin Tomáška [a], Ignác Bugár [a,d]

[a] Slovak Centre of Scientific and Technical Information, Lamačská cesta 8 A, Bratislava, 840 05, Slovakia
[b] Research Centre for Microtechnology, Vorarlberg University of Applied Sciences, Hochschulstraße 1, Dornbirn, 6850, Austria
[c] Institute of Electronics and Photonics, Slovak University of Technology, Ilkovičova 3, Bratislava, 84104, Slovakia
[d] Institute of Chemistry and Environmental Sciences, University of Ss. Cyril and Methodius in Trnava, Nam. J. Herdu 2, Trnava, 91700, Slovakia

ARTICLE INFO

Keywords:
Cyclic AWG
ITU-T grid
Athermal waveguide
Dispersion
Wavelength routing
DWDM

ABSTRACT

Cyclic arrayed waveguide gratings (CAWGs) are widely used as multi-band wavelength routers in integrated photonic systems, where accurate alignment to the frequency-defined ITU-T DWDM grid is essential. In this work, we present a calibration-oriented analysis of ITU-T grid alignment in athermal CAWGs, focusing on practical design and optimisation aspects. An equation-level linear–quadratic output-plane mapping model is introduced, enabling independent control of channel spacing, dispersion-induced curvature, and absolute spectral positioning without modifying the intrinsic CAWG core geometry. Based on this model, a systematic four-stage calibration workflow is developed, allowing near-ITU conformity to be achieved within the selected design cycle C1. The results further demonstrate that simultaneous alignment across multiple cyclic replicas remains fundamentally constrained by order-dependent free spectral range behaviour. This provides a clear distinction between correctable mapping artefacts and intrinsic device limitations. In addition, temperature robustness is evaluated using the normalised temperature-dependent centre-wavelength shift over a wide temperature range, confirming stable performance of the athermal design and revealing cycle-dependent behaviour. The presented approach provides a practical framework for calibration-ready CAWG design and offers insight into the inherent trade-offs in multi-cycle wavelength routing systems.

1. Introduction

Cyclic arrayed waveguide gratings (CAWGs) are compact wavelength routing components that enable periodic replication of a demultiplexing function across multiple spectral cycles, making them attractive for broadband wavelength routing in next-generation optical access architectures such as Super-PON (DeSanti et al., 2020). In these systems, multiple cyclic bands spanning the C and L telecommunication regions must be routed with high spectral accuracy, typically with respect to a frequency-defined ITU-T DWDM grid (Union, 2020). Achieving robust grid alignment in a CAWG is, however, complicated by two coupled effects: (i) the temperature dependence of the AWG spectral response and (ii) the intrinsic wavelength dependence of the free spectral range (FSR) and spectral magnification in cyclic operation.

Arrayed waveguide gratings and PHASAR-based wavelength routers are well-established integrated-optical components for wavelength multiplexing, demultiplexing and routing. Their operation relies on the combined dispersive action of the phased-array section and the imaging properties of the free-propagation regions (FPRs), which map wavelength-dependent phase differences onto spatially separated output positions (Smit and van Dam, 1996; Leijtens et al., 2006). In addition to conventional AWG layouts, numerous custom AWG designs have been reviewed and developed to improve application-specific performance metrics (van Wijk et al., 2023), including spectral resolution (Zhang et al., 2023), passband shape and bandwidth (van Wijk et al., 2020), loss uniformity and output-waveguide configuration (Yuan et al., 2023; Yang et al., 2024). Other geometry- and imaging-level approaches include aberration-theory-based optimisation using non-standard or stigmatic-point geometries (Wang et al., 2001) and FPR imaging or defocus-related correction strategies (Stoll et al., 2017). These approaches typically act at the physical-layout, imaging, or transmission-response design level, whereas the present work focuses on a compact calibration-oriented mapping model for separating correctable output-plane mapping errors from intrinsic cyclic-order-dependent residuals.

Conventional AWGs exhibit substantial temperature-dependent centre-wavelength shift (TD-CWS), which limits deployment in outdoor

* Corresponding author.
E-mail address: jozef.chovan@cvtisr.sk (J. Chovan).
URL: https://www.cvtisr.sk (J. Chovan).

https://doi.org/10.1016/j.rio.2026.101121
Received 1 June 2026; Received in revised form 9 July 2026; Accepted 3 August 2026
Available online 18 August 2026
2666-9501/© 2026 The Authors. Published by Elsevier B.V. This is an open access article under the CC BY license (http://creativecommons.org/licenses/by/4.0/).

or otherwise uncontrolled environments where active thermal stabilisation is undesirable. Athermal operation can be realised by engineering the waveguide thermo-optic response such that the effective index change compensates thermal expansion, thereby suppressing the first-order temperature dependence of the interference condition. In our platform, a silicon oxynitride (SiOxNy/SiON) core combined with a PMMA over-cladding provides opposing thermo-optic coefficients, enabling a fabrication-tuneable athermal waveguide for the phased-array section. This approach reduces TD-CWS in the design band and forms a practical basis for passive thermal robustness in CAWG wavelength routers.

For wide-temperature-range operation, previous athermal AWG studies have shown that residual second-order temperature dependence can become important; for example, second-order compensation in a silica-based athermal AWG reduced the passband wavelength variation over the −40 °C to +80 °C range (Kamei et al., 2009b). More generally, athermal waveguide design can also be combined with dispersion engineering, as demonstrated in hybrid waveguide platforms providing near-zero effective thermo-optic response over a broad wavelength range (Ma et al., 2022).

Even for an athermal CAWG, however, simultaneous ITU-T grid alignment across all cyclic bands is fundamentally constrained. In a cyclic AWG, each spectral band corresponds to a different interference order, and the mapping from output-plane angle to wavelength is order-dependent. Moreover, the dependence of FSR width on wavelength scales with λ^2 since it is related to the group index $n_g(\lambda, T)$. Thus, a frequency-uniform grid cannot be perfectly reproduced across multiple orders using a single fixed geometry and uniform port pitch. In practice, this manifests as a residual, cycle-dependent misalignment that increases with interference order; after calibrating the design cycle C1, the remaining cycles exhibit progressively larger offsets, consistent with the intrinsic order-dependent behaviour of CAWGs.

Frequency-grid conformity in AWGs is closely related to the distinction between constant wavelength spacing and constant frequency spacing. In DWDM-oriented AWG design, centre-frequency accuracy can be degraded when the output-channel positions are generated from a constant wavelength increment rather than from a frequency-defined grid; this effect becomes cumulative in high-channel-count devices and can lead to larger errors near the edge channels (Tang et al., 2023). For cyclic AWG routers, similar grid-deviation issues are particularly relevant because the operating frequencies of repeated cyclic channels may deviate from the standardised frequency grid when the FSR is large (Fan et al., 2021).

A second, equally important practical challenge is that the as-designed output-plane port placement produced by standard synthesis workflows typically assumes a strictly linear channel-to-angle mapping. Residual material and waveguide dispersion introduce a weak but systematic nonlinear curvature of centre-wavelength shift (CWS) across channels, such that a purely linear mapping cannot simultaneously deliver correct channel spacing and minimal curvature within the design cycle C1. This motivates a calibration strategy that acts directly at the level of the output-plane angle mapping, without changing the intrinsic CAWG core geometry, namely a linear scale factor S to restore the effective channel spacing, a quadratic correction c_2 to compensate curvature arising from dispersion, and a global angular offset Z_{corr} to re-centre the band.

In this paper, we present a design- and calibration-oriented study of a 20-channel, 100 GHz athermal CAWG designed for Super-PON (De-Santi et al., 2020) operation across four cyclic replicas (C2, C1, L2 and L1). Building on our earlier work on athermal SiON/PMMA waveguide engineering and dispersion characterisation (Chovan et al., 2025), we focus here on a practical mapping-correction workflow that (i) isolates slope, curvature and absolute-centre errors, (ii) achieves near-grid alignment in the design cycle C1, and (iii) quantifies the residual inter-cycle misalignment that persists due to order-dependent FSR behaviour. Importantly, we emphasise the separation between correctable layout-mapping errors and inherently uncorrectable order-dependent offsets in cyclic AWGs, providing a physics-consistent interpretation of what mapping calibration can and cannot achieve for a fixed CAWG geometry.

Table 1
Main design parameters of the simulated 20-channel, 100 GHz athermal CAWG.

Parameter	Value
Number of output channels	20
Number of input channels	1
Channel spacing	100 GHz
Reference/design cycle	C1
Analysed cyclic replicas	C2, C1, L2, L1
Central/reference wavelength	1555.35 nm
Free spectral range	2.2 THz
Path-length difference	87.387 μm
Number of arrayed waveguides	55
Diffraction order	86
Output waveguide pitch	7.5 μm
FPR front radius	614.216 μm
FPR back radius	1228.433 μm
Arrayed-waveguide pitch	7.5 μm
Minimum bending radius	500 μm

The remainder of the paper is organised in six sections. After a short introduction in Section 1, the simulation framework and the extraction of centre wavelengths and ITU-T grid offsets from Synopsys AWG Utility power-normalised transfer-matrix data are described in Section 2. The output-plane angle mapping model and the linear–quadratic calibration parameters (S, c_2, Z_{corr}) are introduced in Section 3. Section 4 presents alignment results for the design and non-design cycles, including channel-spacing restoration and residual-misalignment trends across cyclic replicas, together with a summary of temperature-robustness results described in Section 4.4. The order-dependent limitation imposed by FSR behaviour in cyclic operation is then discussed in Section 5. Finally, Section 6 concludes with practical implications for calibration-ready CAWG designs for broadband access networks.

2. Methods/simulation setup

2.1. Device model and simulation tool

The spectral response of the 20-channel, 100 GHz athermal cyclic AWG was simulated using Synopsys AWG Utility (BeamPROP), with excitation applied at input port 1 and the responses recorded at all 20 output ports over a wavelength span covering the four cyclic replicas C2, C1, L2 and L1. Unless otherwise stated, the baseline results are reported for the nominal temperature of 20 °C. The simulation output was exported in TransferMatrixFormat1 (POWER), yielding power-normalised transfer data for each output port as a function of wavelength. The simulated wavelength span was 1527.35–1601.75 nm, sampled with 4465 uniformly spaced spectral points ($\Delta\lambda \approx 16.7$ pm per step). Fig. 1 shows the simulated multi-cycle transmission spectra (input port 1, all 20 output ports), which serve as the basis for all subsequent post-processing and calibration steps. To improve reproducibility of the device model, the main CAWG design parameters are summarised in Table 1. These parameters define the intrinsic device geometry and remain fixed throughout the mapping-calibration procedure.

2.2. Power normalisation

Power transmission is reported in decibels as a power ratio

$$T(\lambda) = 10\log_{10}\left(\frac{P_{\mathrm{out}}(\lambda)}{P_{\mathrm{in}}(\lambda)}\right)\ \mathrm{dB} \tag{1}$$

where P_{out} is the output power at a given port and P_{in} is the input power. In the exported power transfer-matrix format, the data are

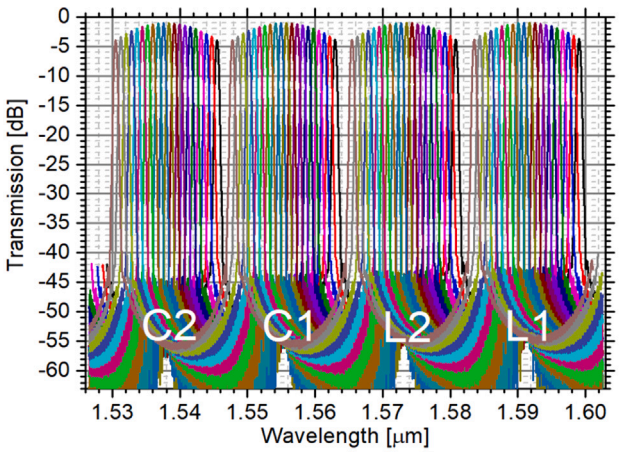


Fig. 1. Simulated power-transmission spectra of the 20-channel, 100 GHz athermal cyclic AWG at 20 °C for excitation at input port 1 and detection at all 20 output ports.

power-normalised with P_{in} taken as unity for the selected excitation, such that the reported traces correspond to $10\log_{10}(P_{out})$ referenced to the input port.

2.3. Centre-wavelength extraction and ITU-T grid offset metric

For each output channel and each cyclic replica, the centre wavelength (CW) was extracted from the simulated passband as the mean of the two boundary wavelengths at which the transmission drops by 3 dB relative to the passband peak (left and right −3 dB points). The CW alignment error was quantified as the CW-offset relative to the ITU-T DWDM frequency grid (Union, 2020), expressed in picometres for each channel index and each cyclic replica.

2.4. Spectral sampling and numerical refinement

To improve numerical localisation of the −3 dB crossing points, an interpolation-based sub-sample refinement procedure was applied during CW extraction. In the initial processing workflow, the CW was estimated as the mean wavelength of all native spectral samples lying above the −3 dB threshold. This approach was found to be sensitive to the finite spectral sampling step, because the extracted CW could depend on which discrete wavelength samples happened to fall inside the −3 dB passband.

In the final extraction procedure used in this work, each passband peak was first identified on the native spectral grid. The peak wavelength and peak power were refined using a local parabolic fit to the peak sample and its two neighbouring samples. The −3 dB threshold was then defined relative to this peak level. The left and right −3 dB crossing wavelengths were obtained by linear interpolation between the adjacent spectral samples surrounding each crossing. The CW was finally calculated as the arithmetic mean of these two interpolated crossing wavelengths. This procedure reduces discretisation effects in the CW extraction while preserving the intrinsic resolution of the original simulation data.

2.5. Dispersion inputs and outputs used in later sections

The simulated CAWG response includes wavelength-dependent waveguide behaviour through the athermal SiON/PMMA platform (Yin et al., 2012; Trenti et al., 2018; Beadie et al., 2015); supporting waveguide information (athermal operating point and waveguide cross-section) is provided in Supplementary Figs. S1 and S2. Material dispersion and the waveguide effective and group-index dependencies relevant to FSR behaviour are summarised in Supplementary Figs. S3–S5. The extracted CW-offsets versus channel index (Figs. 2 and 4), the derived channel-spacing behaviour (Fig. 5), and the temperature-dependent shifts (Fig. 6) were all computed from the same power-normalised transfer-matrix spectra described above, ensuring consistent metrics throughout the calibration workflow.

2.6. Temperature conditions and TD-CWS definition

Temperature robustness was evaluated at absolute temperatures of −40 °C and +80 °C, using 20 °C as the reference condition. These temperatures correspond to excursions of −60 °C and +60 °C, respectively, relative to the reference temperature. The temperature-dependent centre-wavelength shift was defined, for each channel and cycle, as:

$$\Delta\lambda(T) = \lambda_{CW}(T) - \lambda_{CW}(20\,^{\circ}\mathrm{C}) \tag{2}$$

Supplementary material related to this article is available online and includes additional waveguide and dispersion data (Supplementary Figs. S1–S6).

3. Calibration model (Angle mapping)

The CAWG channel centres are ultimately determined by the phase-matched interference condition in the phased array, while the assignment of each wavelength channel to a physical output port is governed by the output FPR imaging and by the angular placement of the output waveguides at the output focal arc. In practice, the layout synthesis workflow provides a nominal channel-to-angle mapping that places output ports at (approximately) uniform angular increments. In this work, the calibration is performed at the mapping-equation level: the intrinsic CAWG core geometry is kept unchanged, while the port-angle mapping is parameterised such that (i) the effective channel spacing, (ii) the residual curvature across the channel set, and (iii) the absolute centring of a chosen reference cycle can be tuned independently. It should be emphasised that the proposed correction is applied at the level of the output-port angular mapping and does not modify the intrinsic CAWG core geometry. The phased-array section, path-length difference, diffraction order, FPR geometry and underlying waveguide layout are kept fixed. The function $\theta(X)$ therefore represents a reparameterisation of the relationship between the output-port index X and the angular coordinate used for spectral mapping and calibration. In this sense, the method should be understood as a mapping-level calibration rather than a full geometric re-optimisation of the CAWG layout. The present section defines the baseline ("original") mapping used by the synthesis tool and establishes the reference against which the corrected mapping is introduced in Section 3.2.

3.1. Baseline mapping (Original)

Let $X \in \{1, \ldots, 20\}$ denote the output-port (channel) index and let X_0 denote the centre index of the output array. For an even channel count, X_0 is the half-sum of the first and last indices; for twenty channels, $X_0 = 10.5$. In the baseline mapping produced by the design utility, the angular position of output port X at the output focal arc is prescribed by a strictly linear channel-to-angle relation, which can be written in the centred form

$$\theta(X) = 180^{\circ} - A_i\,(X - X_0) \tag{3}$$

where A_i is a geometry-dependent constant that sets the nominal angular pitch per channel. Eq. (3) enforces a uniform angular pitch $\Delta\theta \approx A_i$ across the output array, i.e. a constant increment in $\theta(X)$ for successive channel indices. This baseline assumption is appropriate if the output FPR provides (approximately) linear imaging and if the local spectral sensitivity $\mathrm{d}\lambda/\mathrm{d}\theta$ is constant over the relevant angular

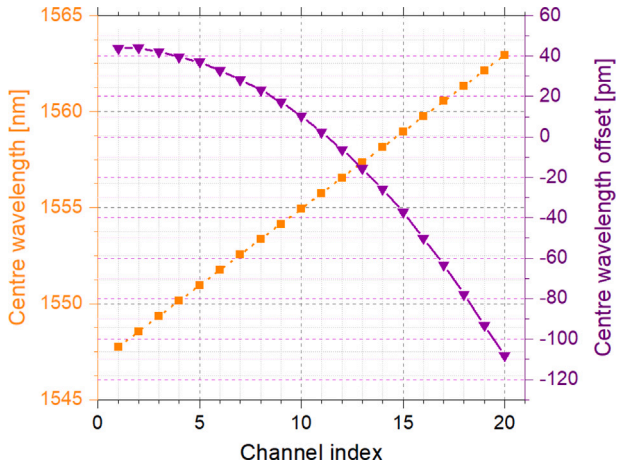


Fig. 2. Original wavelength distribution of the 20 CAWG output ports with constant spacing in the C1 cycle, showing (left) absolute CWs and (right) CW-offsets.

span. In a cyclic AWG, however, $\mathrm{d}\lambda/\mathrm{d}\theta$ is not strictly constant because it depends on both wavelength and interference order; consequently, a strictly uniform port pitch maps into a wavelength spacing that is only approximately uniform within a given cycle and cannot simultaneously reproduce a frequency-uniform ITU-T grid across multiple cycles.

From a calibration perspective, Eq. (3) therefore represents the baseline reference case in which (i) the channel-spacing error manifests primarily as an effective slope error in channel index versus wavelength, and (ii) residual dispersion produces a weak but systematic non-linearity in the centre wavelengths across channels. These baseline behaviours are quantified later in the paper using the extracted ITU-T grid centre-wavelength offsets (Figs. 2 and 4) and the derived channel spacing (Fig. 5).

Finally, it is useful to interpret Eq. (3) geometrically. The output ports lie on (or near) a circular focal arc of radius R_0, so a uniform angular pitch corresponds to a uniform arc-length spacing $s \approx R_0\,\Delta\theta$ between adjacent output waveguides. Fig. 2 illustrates the detailed CW distribution and corresponding CW-offsets associated with the baseline placement in the C1 cycle, which motivates introducing controlled departures from strict linearity in the corrected mapping.

3.2. Linear–quadratic correction

The baseline mapping in Eq. (3) enforces a strictly linear channel-to-angle relation with an (approximately) uniform angular pitch across the output array. In practice, the simulated CW-offsets and channel-spacing trends (reported later in Figs. 4 and 5) reveal two systematic components that a purely linear mapping cannot remove simultaneously: (i) a slope error corresponding to an effective channel-spacing mismatch, and (ii) a non-linear curvature caused by residual dispersion and a non-constant $\mathrm{d}\lambda/\mathrm{d}\theta$ over the output angular span. To separate these effects in a physically interpretable way, we introduce a linear–quadratic correction to the output-plane angle mapping. Let $X \in \{1, \ldots, 20\}$ be the output-port index and let $X_0 = 10.5$ denote the centred index for twenty channels. The corrected mapping is written in centred form as

$$\theta(X) = 180^\circ - A_i S\,(X - X_0) + c_2\,(X - X_0)^2 + Z_{\mathrm{corr}} \tag{4}$$

where the three parameters have distinct roles. The linear scale S adjusts the effective angular slope of the mapping and therefore restores the target channel spacing in the chosen reference cycle. The quadratic term c_2 introduces a controlled second-order curvature in $\theta(X)$, compensating the systematic non-linearity associated with dispersion and the weak angle dependence of spectral imaging. The global offset Z_{corr} provides a uniform angular rotation that re-centres the selected reference cycle without altering its slope or curvature.

Eq. (4) reduces to the baseline mapping when $S = 1$, $c_2 = 0$, and $Z_{\mathrm{corr}} = 0$. Importantly, this correction acts only at the mapping level (i.e. the channel-to-port assignment at the output FPR) and does not modify the intrinsic phased-array interference condition that sets the underlying periodicity of the CAWG response. As a result, the correction can strongly improve ITU-T grid conformity within a selected design cycle (here, C1), while residual inter-cycle offsets remain governed by order-dependent FSR behaviour.

The proposed correction should be distinguished from layout-level AWG optimisation methods. Existing approaches for improving AWG performance include aberration-theory-based design and non-standard imaging geometries (Wang et al., 2001), FPR imaging and defocus-related correction strategies in high-resolution AWGs (Stoll et al., 2017), and optimisation of output-waveguide configurations to improve loss nonuniformity and crosstalk (Yang et al., 2024). These methods generally modify, or explicitly optimise, physical layout or imaging properties of the AWG.

The present approach is also different from centre-frequency-accuracy optimisation methods that directly adjust the angular spacing and angular position of the output waveguides to match a frequency-defined grid (Tang et al., 2023). Those methods explicitly optimise the physical output-waveguide geometry, for example through parameters such as α_i and β_i. By contrast, the present work uses the three parameters S, c_2, and Z_{corr} as a compact calibration-oriented mapping model. This allows the correctable slope, curvature and common-mode offset contributions to be separated from the residual cyclic-order-dependent mismatch that remains in non-design cycles.

Fig. 2 provides the geometric motivation for Eq. (4). The yellow curve shows the CW placement, while the violet curve shows the CW-offsets relative to the ITU-T grid in the C1 cycle. Departures from perfectly uniform pitch and the associated variation in local imaging sensitivity manifest as curvature-like contributions in the channel-index dependence of the extracted CW-offsets, which are directly targeted by the quadratic term c_2. The subsequent calibration procedure (Section 3.3) exploits the separation of roles in Eq. (4) to tune S, c_2, and Z_{corr} sequentially using the CW-offset and channel-spacing metrics reported in Figs. 4 and 5.

3.3. Four-stage calibration workflow

To calibrate the output-plane mapping in a reproducible and fabrication-friendly manner, we apply a four-stage workflow that isolates three physically distinct contributions to the CW-offset within a chosen reference cycle (here: C1). The workflow operates directly on the mapping parameters of Eq. (4), namely the linear scale S, the quadratic curvature term c_2, and the global angular offset Z_{corr}, such that each step predominantly corrects a single component of the observed mismatch. The calibration objective and its outcome are evaluated using two complementary metrics derived from the simulated spectra described in Section 2: (i) CW-offset from the ITU-T grid (Fig. 4) and (ii) channel-spacing behaviour relative to the ITU-T grid (Fig. 5).

Stage 0 — Baseline response (original mapping). As a starting point, the baseline mapping of Eq. (3) is used, corresponding to Eq. (4) with

$$S = 1, \quad c_2 = 0, \quad Z_{\mathrm{corr}} = 0 \tag{5}$$

The resulting CW-offset pattern in the reference cycle provides a diagnostic "signature" of the mapping error: a dominant linear trend indicates an effective channel-spacing (slope) mismatch, while a weak systematic curvature indicates dispersion-induced non-linearity not captured by the linear mapping.

Stage 1 — Slope (spacing) correction via the linear scale. S. In the first correction step, only the linear scale is enabled ($S \neq 1$, $c_2 = 0$, $Z_{\mathrm{corr}} = 0$) to restore the target 100 GHz channel spacing in the reference cycle. Practically, S is tuned until the per-channel spacing inferred from adjacent CWs matches the ITU-T grid spacing most closely (Fig. 5), equivalently minimising the residual linear slope in the CW-offset curve (Fig. 4). For the present design, this step yields a small correction S close to unity, consistent with a modest scaling error in the original output-plane port pitch.

Stage 2 — Curvature correction via the quadratic term. c_2. With the spacing corrected, the remaining systematic deviation in the reference cycle typically appears as a non-linear curvature of the CW-offset versus channel index. In the second correction step, the quadratic term is enabled ($c_2 \neq 0$, with S fixed from Stage 1 and $Z_{\mathrm{corr}} = 0$) to suppress this curvature without re-introducing a slope error. The parameter c_2 is tuned to minimise the residual second-order component of the CW-offset profile in the reference cycle (Fig. 4), which simultaneously flattens the channel-spacing deviation profile across all four cycles (Fig. 5). For the device analysed here, a small negative c_2 compensates the residual dispersion-driven curvature observed under the baseline mapping. A small uniform deviation may still remain across all channels; however, it is negligible at the scale of the plotted curves and is compensated in the next stage.

Stage 3 — Absolute centring via the global offset. Z_{corr}. After slope and curvature have been corrected, a residual common-mode shift of the entire reference cycle may remain (i.e. all channels are displaced by the same amount relative to the ITU-T grid). In the final step, Z_{corr} is adjusted (with S and c_2 held fixed) to eliminate this residual bias and to place the reference cycle on the ITU-T grid. Because Z_{corr} corresponds to a uniform angular rotation, it shifts all channels equally and therefore does not alter the corrected CW-offset or channel-spacing curvature. Mathematically, Z_{corr} enters Eq. (4) as an additive angular constant. Therefore, it does not change the first or second derivative of $\theta(X)$ with respect to the channel index X, and hence does not introduce additional slope or curvature in the angular mapping itself. Its primary role is to remove the common-mode CW-offset of the reference cycle. It should be noted, however, that the wavelength response of an AWG is not strictly linear with output angle over an arbitrary large angular range. Therefore, a very large global angular displacement could in principle sample a different local region of the nonlinear wavelength-to-angle response and produce a weak secondary effect on the wavelength-domain spacing. In the present work, the optimised value $Z_{\mathrm{corr}} \approx -0.0057°$ is small, and its effect on channel-spacing curvature is negligible compared with the changes introduced by S and c_2.

Practical remarks and expected outcome. This four-stage procedure provides a compact and deterministic way to calibrate the CAWG output mapping. Stage 0 corresponds to the response of the original mapping, Stage 1 corrects the effective spacing (slope), Stage 2 corrects dispersion-related curvature, and Stage 3 sets the absolute spectral origin of the chosen reference cycle. When applied to the C1 cycle, the method yields near-grid conformity in C1, while the remaining cycles retain order-dependent residual offsets that cannot be removed simultaneously by any single static mapping applied to a fixed-geometry CAWG (discussed in Section 5 with reference to Fig. 7). For the present device, the calibration converged to $S \approx 1.0047$, $c_2 \approx -3.5 \times 10^{-4}$, and $Z_{\mathrm{corr}} \approx -0.0057°$ for the C1 reference cycle. Fig. 3 shows the resulting optimised output-plane angular placement of the 20 CAWG output ports.

3.3.1. Implementation details: Metrics and numerical procedure

The four-stage calibration described above was implemented as a deterministic, metric-driven tuning loop operating on the CW-offsets extracted from the Synopsys AWG Utility spectra (Section 2). The optimisation was realised using Python-based fitting procedures. Two complementary metrics were evaluated for the C1 reference cycle after each parameter update: (i) the CW-offset from the ITU-T DWDM grid (Union, 2020) (Figs. 2 and 4) and (ii) the channel-spacing deviation relative to the ITU-T grid (Fig. 5).

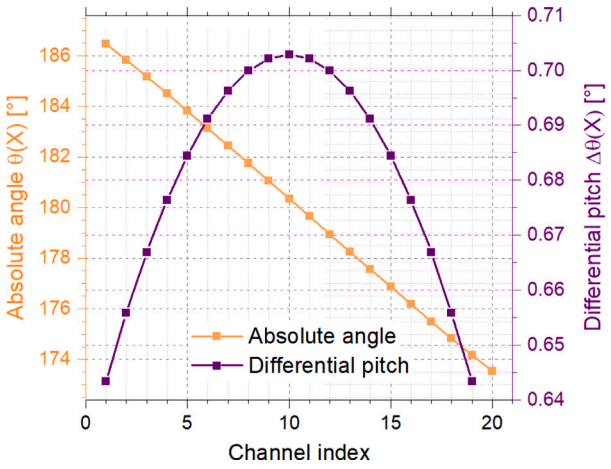


Fig. 3. Output-plane angular placement of the 20 CAWG output ports, showing the absolute angle $\theta(X)$ and the differential pitch $\Delta\theta(X)$ between neighbouring ports.

(a) CW-offset metric (grid misalignment): For each channel index X, the CW-offset was defined as

$$\Delta\lambda_X = \lambda_{\mathrm{CW},X} - \lambda_{\mathrm{ITU},X} \tag{6}$$

where $\lambda_{\mathrm{CW},X}$ is the centre wavelength extracted from the simulated passband using the mean of the two −3 dB points (Section 2.3), and $\lambda_{\mathrm{ITU},X}$ is the corresponding ITU-T grid wavelength. The offset curve $\Delta\lambda_X$ (Fig. 4) was used both as a diagnostic (slope and curvature) and as an optimisation target.

(b) Channel-spacing metric (slope/spacing error): The local channel spacing within a cycle was evaluated from adjacent CWs as

$$\Delta\lambda_X^{(\mathrm{ch})} = \lambda_{\mathrm{CW},X+1} - \lambda_{\mathrm{CW},X}, \quad X = 1, \ldots, 19 \tag{7}$$

and compared against the ITU-T grid spacing expressed in wavelength units at the local wavelength (Fig. 5). This metric is directly sensitive to the linear scale factor S in Eq. (4) and was therefore used as the primary indicator in Stage 1.

(c) Parameter-tuning rules per loop: **Stage 1 (tuning S) — slope removal.** With $c_2 = 0$ and $Z_{\mathrm{corr}} = 0$, S was adjusted to minimise the residual linear trend in $\Delta\lambda_X$ and to bring $\Delta\lambda_X^{(\mathrm{ch})}$ closest to the ITU-T grid spacing across the C1 channels (Figs. 4 and 5).

Stage 2 (tuning c_2) — curvature removal. With S fixed from Stage 1 and $Z_{\mathrm{corr}} = 0$, c_2 was adjusted to minimise the second-order (curvature) component of $\Delta\lambda_X$, equivalently flattening the residual nonlinearity visible in Fig. 4 and reducing the non-uniformity observed in Fig. 5.

Stage 3 (tuning Z_{corr}) — absolute centring. With S and c_2 fixed, Z_{corr} was set to remove the remaining common-mode bias of the C1 cycle, i.e. to make the mean (or centre-channel average) CW-offset in Fig. 4 as close to zero as possible. Performing these three stages constitutes one tuning loop, which was iteratively repeated to achieve convergence of the parameters to the fourth decimal place. A local sensitivity test for Z_{corr}, showing that it primarily introduces a common-mode CW-offset shift without practically changing the corrected curvature, is provided in Supplementary Fig. S8.

(d) Numerical considerations: Because the native spectral sampling is discrete and the CW extraction relies on −3 dB points, CW localisation is affected by sampling granularity; therefore, interpolation-based sub-sample refinement was applied during CW extraction (Section 2.4). This refinement improves the stability of $\Delta\lambda_X$ and $\Delta\lambda_X^{(\mathrm{ch})}$ as optimisation metrics while remaining consistent with the intrinsic resolution of the underlying simulation data.

(e) Scope of calibration: All parameters (S, c_2, Z_{corr}) were optimised using the C1 reference cycle only; the resulting mapping was then applied unchanged to the remaining cycles (C2, L2 and L1) to quantify the residual inter-cycle misalignment constrained by cyclic order-dependent behaviour. For absolute centring in Stage 3, the residual common-mode bias was evaluated at the C1 band centre defined as the average of channels 10 and 11 (i.e. $X_0 = 10.5$), and Z_{corr} was adjusted to drive the mean offset of channels 10–11 to zero.

4. Results: ITU-grid alignment and residuals

This section reports the alignment performance of the 20-channel, 100 GHz athermal CAWG with respect to the ITU-T DWDM grid (Union, 2020), using the CW extraction and metrics defined in Section 2 and the mapping-calibration model from Section 3. The results are presented for all four cyclic replicas (C2, C1, L2 and L1) at the nominal temperature of 20 °C, comparing the baseline ("original") output-plane mapping with the calibrated ("corrected") mapping obtained by sequential tuning of S, c_2, and Z_{corr} in the C1 reference cycle. Cyclic AWG and AWGR devices have previously been demonstrated in several wavelength-routing contexts, including silicon photonic and cyclic-frequency router implementations (Pitris et al., 2018; Kamei et al., 2009a). In such devices, frequency-grid deviations and cycle-dependent behaviour are important practical design constraints, motivating the present analysis of ITU-T grid conformity across multiple cyclic replicas.

4.1. CW-offset vs. ITU-T grid (Original vs. Corrected)

Fig. 4 shows the CW-offset from the ITU-T DWDM grid (Union, 2020) as a function of channel index for all four cyclic replicas, plotted for both the original ("or") and corrected ("co") output-plane mappings. Under the original mapping, the dominant feature is a systematic channel-dependent trend within each cycle, consistent with a slope error in the channel-to-angle mapping (Stage 1 in Section 3.3), accompanied by a weaker non-linear component attributable to dispersion-induced curvature (Stage 2).

After applying the calibrated mapping, the reference cycle (C1) is visibly re-aligned towards the ITU-T grid across the full channel set, reflecting the separation of roles in Eq. (4): the scale factor S restores the effective channel spacing, the quadratic term c_2 suppresses the systematic curvature, and the global offset Z_{corr} re-centres the band. A further notable effect of the correction is the removal of the non-linear curvature in all cycles. However, as expected for a fixed-geometry CAWG, the non-design cycles (C2, L2 and L1) retain residual offsets even after C1 is corrected; these residuals increase with cyclic order and are discussed in Section 5 in terms of order-dependent FSR behaviour (Fig. 7). This behaviour is consistent with previous observations in AWG and cyclic-AWGR designs, where frequency-grid deviations can arise from the mismatch between wavelength-domain design parameters and frequency-domain grid requirements (Tang et al., 2023), and where cyclic-router operation can exhibit channel deviations from the standardised grid when the effective FSR is large (Fan et al., 2021). Similar frequency-deviation and cyclic-order effects have also been reported in cyclic AWG/AWGR routing structures, where maintaining grid conformity across repeated spectral replicas remains a non-trivial design challenge (Kamei et al., 2009a; Idris et al., 2014).

It should be noted that the absolute magnitude of "small" residuals is ultimately bounded by the numerical CW-localisation procedure. The simulated spectra are sampled on a discrete wavelength grid, and CWs are extracted from −3 dB points. The interpolation-based sub-sample refinement improves the numerical localisation of the −3 dB crossing points, but does not provide metrological accuracy beyond the intrinsic simulation resolution. Consequently, single-digit picometre residuals reported for the corrected C1 cycle should be interpreted as a measure of the correction capability of the mapping model within the simulation framework, rather than as an absolute fabrication-level performance guarantee.

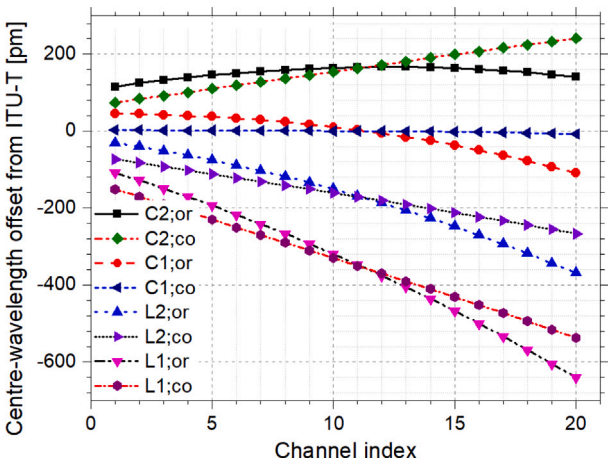


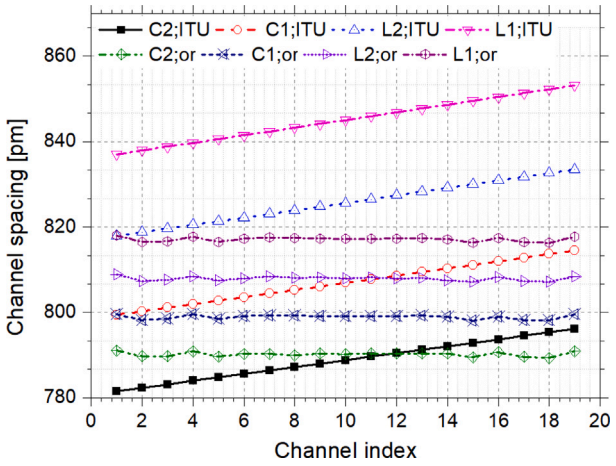
Fig. 4. Simulated CW-offset from the ITU-T DWDM grid (Union, 2020) for the 20-channel, 100 GHz cyclic AWG at 20 °C, shown as a function of channel index for the four cyclic replicas (C2, C1, L2 and L1). For each cycle, results are shown for the original ("or") and corrected ("co") output-plane angle mapping, as indicated in the legend.

4.2. Channel-spacing vs. ITU-T grid (Mapping effect)

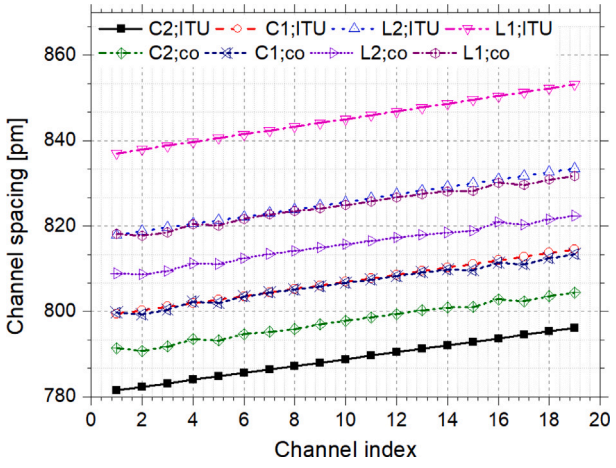
While Figs. 2 and 4 quantify the absolute CW alignment, the effect of the mapping correction is more directly diagnosed through the channel-spacing behaviour. Fig. 5 compares the channel spacing derived from adjacent CWs against the ITU-T grid spacing for all four cyclic replicas, shown for (a) the original mapping and (b) the corrected mapping. In Fig. 5(a), the channel spacing exhibits a systematic deviation from the ITU-T grid target, consistent with an effective scaling error in the baseline channel-to-angle mapping. After applying the linear–quadratic correction, Fig. 5(b) shows that the spacing within the reference cycle is restored much closer to the ITU-T target over the full channel set, confirming that the scale factor S predominantly controls the slope (Stage 1), while the quadratic term c_2 removes the residual curvature (Stage 2) without re-introducing a spacing error. Importantly, Fig. 5(b) also clarifies the practical limit of a single mapping calibration: once curvature-related deviations are suppressed in the reference cycle, the remaining inter-cycle differences are largely systematic and cannot be eliminated simultaneously across all four cycles using a single static output-plane mapping applied to a fixed-geometry CAWG. This observation is consistent with previous cyclic AWGR studies, where performance improvements were achieved through architectural or layout-level modifications, but cycle-dependent frequency deviations remained an important design consideration (Kamei et al., 2009a; Zhang et al., 2025).

4.3. Summary of calibration outcome across cycles (Link to physical limitation)

Taken together, Figs. 4 and 5 demonstrate that the mapping-equation correction provides strong control over the two dominant correctable components of the alignment error within the reference



(a) Original output-plane angle mapping.



(b) Output-plane mapping after linear–quadratic correction.

Fig. 5. Channel spacing as a function of channel index, compared with the ITU-T DWDM grid (Union, 2020) for the four cyclic replicas (C2, C1, L2 and L1).

cycle, namely a channel-spacing (slope) mismatch and a dispersion-related curvature term. The calibrated mapping can therefore deliver near-ITU conformity in the chosen design cycle C1, while the residual offsets in the non-design cycles remain governed by the intrinsic physics of cyclic AWGs rather than by the available mapping degrees of freedom. In the next section, these residual trends are linked to the order-dependent FSR behaviour of the CAWG, explaining why complete multi-cycle ITU-T grid alignment is fundamentally constrained for a fixed-geometry implementation (Fig. 7). The present results therefore complement earlier cyclic AWG/AWGR demonstrations by explicitly separating mapping-correctable alignment errors in the reference cycle from residual cycle-dependent offsets that originate from the cyclic-order-dependent spectral response (Pitris et al., 2018; Kamei et al., 2009a; Idris et al., 2014).

4.4. Temperature robustness (TD-CWS)

All optimisation results in Sections 4.1–4.3 are reported at the nominal temperature of 20 °C, which serves as the reference condition for both the CW-offset metric (Figs. 2 and 4) and the channel-spacing metric (Fig. 5), and also represents the calibration point for the mapping parameters (S, c_2, Z_{corr}) in the C1 reference cycle. The calibration parameters S, c_2, and Z_{corr} were optimised at the reference temperature of 20 °C and then kept fixed for all temperature cases. Thus, the temperature analysis does not represent a temperature-adaptive recalibration, but rather quantifies the temperature-induced deviation from the calibrated 20 °C operating point.

The original and corrected mappings primarily differ in their absolute ITU-grid alignment and channel-spacing behaviour at the reference temperature. However, the TD-CWS is evaluated relative to the corresponding 20 °C centre wavelength obtained with the same mapping configuration. Consequently, any static mapping-induced offset cancels in the TD-CWS calculation, and the reported temperature drift mainly reflects the waveguide thermo-optic and dispersion response rather than changes in the mapping parameters. A direct comparison of the C1 TD-CWS obtained with the original and corrected mappings is provided in Supplementary Fig. S9; the practically overlapping curves confirm that the mapping correction does not introduce an additional temperature drift. To place these 20 °C alignment results in context, we note that the CAWG is implemented on an athermal SiON/PMMA waveguide platform; the athermal operating point and supporting waveguide and dispersion data used in the simulation framework are provided in Supplementary Figs. S1–S5. This interpretation is consistent with earlier athermal AWG and waveguide studies, where both residual higher-order temperature dependence and waveguide-level thermo-optic/dispersion engineering were shown to be relevant for maintaining wavelength stability over broad temperature ranges (Kamei et al., 2009b; Ma et al., 2022).

Temperature robustness is assessed using the TD-CWS definition given in Section 2.6. The shifts are evaluated at absolute temperatures of −40 °C and +80 °C, referenced to 20 °C, and are reported in a normalised form to enable direct comparison across cycles and across the full set of 20 output channels.

4.4.1. Normalised TD-CWS trends across cyclic replicas

Fig. 6 summarises the normalised TD-CWS trends for the four cyclic replicas (C2, C1, L2 and L1) as a function of channel index. The curves provide a compact view of thermal stability, showing how the centre wavelengths of all channels shift relative to their 20 °C positions at the absolute temperatures of −40 °C and +80 °C.

In the design cycle C1, the TD-CWS remains comparatively suppressed across the channel set, consistent with the intended athermal behaviour of the SiON/PMMA waveguide platform near the reference wavelength region. The normalised TD-CWS values lie in the range 0.70–0.81 pm/°C. By contrast, the non-design cycles (C2, L2 and L1) exhibit larger and more systematic temperature-dependent shifts (for C2 and L2 in the range 0.79–1.00 pm/°C; for L1 in the range 1.02–1.24 pm/°C), reflecting that athermal compensation is optimised around the design band, whereas outside this region residual wavelength- and temperature-dependent dispersion remains.

Separated TD-CWS plots for all cycles and for both extreme temperatures are provided in Supplementary Fig. S6 for completeness and ease of comparison. In summary, the mapping optimisation at 20 °C (Figs. 4 and 5) can be interpreted as a representative operating snapshot, while Fig. 6 (and Supplementary Fig. S6) quantifies the temperature-induced deviations from this snapshot across all cycles and channels.

4.4.2. Link to waveguide dispersion inputs

The observed temperature behaviour in Fig. 6 follows from the residual thermo-optic and dispersion response of the athermal SiON/PMMA waveguide platform. The supporting material-dispersion, effective-index and group-index data are provided in Supplementary Figs. S1–S5. These data support the interpretation that first-order thermal drift is mitigated near the design band, while wavelength-dependent dispersion and order-dependent cyclic behaviour continue to influence the multi-cycle response under temperature excursions.

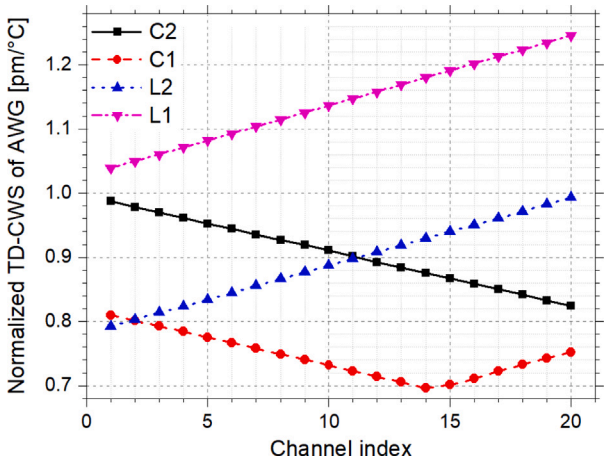


Fig. 6. Normalised TD-CWS referenced to 20 °C for cycles C2, C1, L2 and L1, plotted versus channel index at absolute temperatures of −40 °C and +80 °C. These correspond to temperature excursions of −60 °C and +60 °C relative to the reference condition.

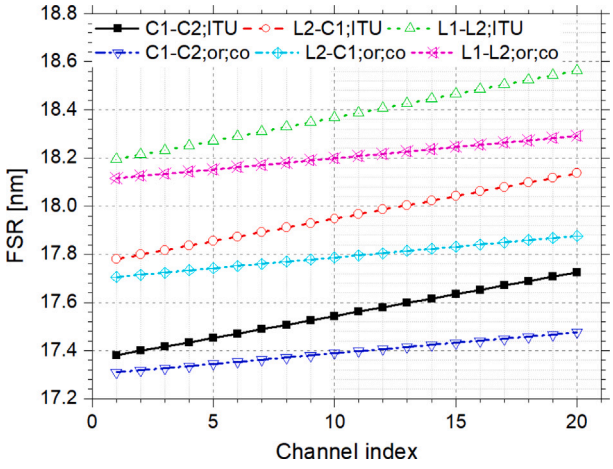


Fig. 7. Comparison of the FSR between the ITU-T DWDM grid (Union, 2020) and the simulated cyclic AWG channel set for the neighbouring cyclic replicas C2, C1, L2 and L1, for both the original and corrected mappings.

5. Discussion

5.1. Fundamental (Order-dependent) limitation

The results in Figs. 4 and 5 show that the mapping correction in Eq. (4) provides strong control over the two dominant, correctable contributions to the alignment error within the selected reference cycle, namely a channel-spacing (slope) mismatch corrected by S and a systematic curvature corrected by c_2, while Z_{corr} sets the absolute spectral origin.

However, the same figures simultaneously reveal that, once the reference cycle is brought close to the ITU-T grid, residual offsets remain in the non-design cycles (C2, L2 and L1). This behaviour is not a limitation of the calibration workflow, but a direct consequence of cyclic AWG physics, in which each cyclic replica corresponds to a different interference order and therefore experiences a different effective spectral mapping.

A CAWG replicates its channel set periodically with a period governed by the FSR, which in wavelength units depends on wavelength through the group index $n_g(\lambda, T)$ and thus on both material and waveguide dispersion. As a result, the relationship between a uniform angular port pitch and the resulting channel positions in wavelength (and equivalently in frequency) is not invariant across interference orders. This effect is quantified in Fig. 7, which compares the ITU-T grid FSR behaviour with the effective CAWG behaviour across cycles and highlights that the effective channel spacing and periodicity are inherently cycle-dependent. Notably, the original and corrected mappings are practically indistinguishable when evaluated at the level of inter-cycle FSR, and are therefore represented by common curves in Fig. 7.

Consequently, calibrating a single mapping function to enforce ITU-T conformity for one cycle cannot simultaneously enforce the same conformity for all cycles in a fixed-geometry CAWG. Once c_2 removes dispersion-related curvature in the reference cycle, the remaining offsets in the other cycles are largely systematic and cannot be eliminated by any single static mapping. In this sense, the mapping correction should be understood as a practical tool that (i) isolates and removes correctable mapping artefacts and (ii) exposes the residual offsets that are intrinsic to cyclic operation and governed by $n_g(\lambda, T)$ and order-dependent imaging sensitivity.

5.2. What cannot be fixed by mapping (fixed geometry)

It is important to distinguish between mapping degrees of freedom and architectural degrees of freedom. In the present approach, the physical layout of the CAWG is unchanged; only the output-plane port-angle mapping is modified through three parameters (S, c_2, Z_{corr}). This means that the intrinsic phased-array interference condition and the underlying periodicity of the device are fixed, and the correction can only redistribute how the existing spectral response is sampled by the output ports. Therefore, the following limitations remain for a fixed-geometry CAWG.

- **Simultaneous multi-cycle ITU-T grid alignment is not achievable with a single static mapping.** Because each cyclic replica corresponds to a different interference order and the effective FSR depends on $n_g(\lambda, T)$, different cycles experience non-uniform spectral magnification and periodicity. A mapping that is optimal for one cycle (C1) cannot be optimal for all cycles simultaneously, as evidenced by the cycle-dependent residual trends in Fig. 4, the cycle-dependent spacing behaviour in Fig. 5, and rationalised by the effective FSR behaviour in Fig. 7.
- **Order-dependent residuals remain even when slope and curvature are removed in the reference cycle.** The separation of roles in Eq. (4) allows slope and curvature to be minimised in the C1 reference cycle, but the remaining residuals in C2/L2/L1 primarily reflect order-dependent behaviour rather than correctable mapping artefacts.
- **Temperature robustness does not remove dispersion-driven inter-cycle offsets.** The athermal waveguide platform suppresses first-order temperature drift near the design band, but wavelength-dependent dispersion and order-dependent cyclic behaviour remain. This is consistent with the TD-CWS trends summarised in Fig. 6 and detailed in Supplementary Fig. S6, as well as with the underlying material and waveguide dispersion inputs provided in Supplementary Figs. S3–S5. Previous athermal AWG and waveguide studies have similarly shown that temperature stabilisation can be improved by device-level or waveguide-level engineering, while residual higher-order temperature dependence and dispersion-related effects may still need to be considered over wide operating ranges (Kamei et al., 2009b; Ma et al., 2022).

Eliminating these limitations would require architectural changes beyond the scope of an equation-level mapping correction. Examples include direct optimisation of output-waveguide angular spacing and position for centre-frequency accuracy (Tang et al., 2023), cyclic-AWGR designs that modify the angular distribution of input and output waveguides near the FPR to reduce channel deviation from the ITU

grid (Fan et al., 2021), aberration-reduced or stigmatic-point AWG geometries (Wang et al., 2001), FPR imaging or field-flattening strategies (Stoll et al., 2017), and modified output-waveguide configurations for improved uniformity or crosstalk performance (Yang et al., 2024). These approaches act directly at the physical-layout, port-distribution, imaging-design, or dispersion-engineering level. In contrast, the present calibration workflow intentionally keeps the intrinsic CAWG core design fixed and adjusts only the compact mapping description used for grid alignment.

The key practical outcome is that a calibration-ready CAWG design can reliably achieve near-ITU conformity in a chosen reference cycle through the mapping workflow, while the remaining cycles exhibit residual offsets determined by cyclic order and dispersion. In practical deployment, the calibrated 20 °C alignment must also remain stable under ambient temperature excursions, which perturb both the waveguide effective and group indices and, consequently, the multi-cycle response.

Although the present study is based on numerical simulations, the proposed calibration workflow is directly applicable to experimentally measured CAWG spectra. In an experimental implementation, the passband spectra measured at the output ports can be processed using the same CW extraction procedure, and the resulting centre wavelengths can be used to determine the mapping parameters S, c_2, and Z_{corr}. Therefore, the method should be regarded as a calibration-ready framework that can be transferred from simulation data to measured device responses once fabricated CAWG samples are available.

6. Conclusions

This paper has presented a design- and calibration-oriented approach to improving ITU-T grid alignment in a 20-channel, 100 GHz athermal cyclic AWG by acting exclusively at the output-plane angle-mapping level, without modifying the underlying CAWG layout. Using Synopsys AWG Utility power-normalised transfer-matrix spectra (Fig. 1), centre wavelengths were extracted consistently and compared against the ITU-T DWDM grid (Union, 2020) to quantify alignment and spacing errors (Figs. 4 and 5). A linear–quadratic mapping correction was introduced to decouple three physically meaningful control parameters: a linear scale factor S to restore channel spacing, a quadratic curvature term c_2 to compensate systematic dispersion-related nonlinearity, and a global angular offset Z_{corr} to re-centre the reference cycle. The corresponding four-stage calibration workflow (baseline → $S \rightarrow c_2 \rightarrow Z_{\mathrm{corr}}$) provides a deterministic procedure for isolating slope, curvature and absolute-centring errors, with centring defined by the average of channels 10–11 in the C1 cycle. As demonstrated by the reduced CW-offsets and improved channel spacing in the design cycle C1, the corrected mapping yields near-ITU conformity within the reference cycle (Figs. 4 and 5). A key outcome is that simultaneous ITU-T grid alignment across all cyclic replicas is fundamentally constrained in a fixed-geometry CAWG: after calibrating one cycle, residual inter-cycle offsets remain and increase with cyclic order due to order-dependent spectral magnification and wavelength-dependent FSR behaviour. This intrinsic limitation is quantified through the effective FSR comparison in Fig. 7 and supported by the dispersion-related waveguide inputs in Supplementary Figs. S3–S5. Finally, temperature robustness was assessed via TD-CWS trends referenced to 20 °C at absolute temperatures of −40 °C and +80 °C, corresponding to temperature excursions of −60 °C and +60 °C (Fig. 6), demonstrating that the calibrated 20 °C alignment can be interpreted as an operating-point snapshot, while temperature-induced deviations relative to this snapshot remain cycle-dependent. The normalised TD-CWS values for the C1 cycle remain below 0.81 pm/°C. By contrast, the non-design cycles (C2, L2 and L1) exhibit larger and more systematic temperature-dependent shifts (for C2 and L2 below 1.00 pm/°C; for L1 below 1.24 pm/°C), reflecting that athermal compensation is optimised around the design band. The athermal operating point and supporting waveguide context are provided in Supplementary Figs. S1 and S2, with additional cycle-resolved TD-CWS trends in Supplementary Fig. S6.

Overall, the presented mapping-equation calibration provides a practical, fabrication-friendly route to calibration-ready athermal CAWGs. It maximises ITU conformity in the selected design cycle C1 while explicitly separating correctable mapping artefacts from the residual order-dependent behaviour inherent to cyclic AWGs.

CRediT authorship contribution statement

Jozef Chovan: Writing – original draft, Software, Methodology, Conceptualization. **Dana Seyringer:** Writing – review & editing, Methodology, Formal analysis. **Anton Kuzma:** Visualization, Software, Investigation. **Martin Tomáška:** Software, Investigation, Data curation. **Ignác Bugár:** Writing – review & editing, Visualization, Methodology, Formal analysis.

Declaration of competing interest

The authors declare that they have no known competing financial interests or personal relationships that could have appeared to influence the work reported in this paper.

Acknowledgements

This work was funded by the EU NextGenerationEU through the Recovery and Resilience Plan for Slovakia under Project No. 09I03-03-V04-00684.

Appendix A. Supplementary data

Supplementary material related to this article can be found online at https://doi.org/10.1016/j.rio.2026.101121.

Data availability

Data will be made available on request.

References

Beadie, G., Brindza, M., Flynn, R.A., Rosenberg, A., Shirk, J.S., 2015. Refractive index measurements of poly(methyl methacrylate) (pmma) from 0.4–1.6 um. Appl. Opt. 54, F139–F143.

Chovan, A., Kuzma, M., Tomáška, F., Uherek, F., 2025. Optimization of rib, single-mode sioxny optical waveguide structure for athermal awg using pmma cover layer. In: Photonics, Devices, and Systems IX. In: SPIE Proceedings, vol. 13698, SPIE, 1369802–1–1369802–7.

DeSanti, C., Du, L., Guarin, J., Bone, J., Lam, C.F., 2020. Super-pon: An evolution for access networks. J. Opt. Commun. Netw. 12, D66–D77.

Fan, Z., Zhao, J., He, J.-J., 2021. High performance demonstration of a 16×16 silica-based cyclic arrayed-waveguide grating router. In: International Conference on Optical Communications and Networks. ICOCN 2021.

Idris, N.A., Asakura, H., Tsuda, H., 2014. Extremely wide-bandwidth cyclic arrayed waveguide grating for waveband routing on t-band and o-band. In: Advanced Photonics for Communications. OSA Technical Digest, Optica Publishing Group, p. JT3A.29. http://dx.doi.org/10.1364/IPRSN.2014.JT3A.29.

Kamei, S., Ishii, M., Kaneko, A., Shibata, T., Itoh, M., 2009a. $n \times n$ cyclic-frequency router with improved performance based on arrayed-waveguide grating. J. Lightwave Technol. 27, 4097–4104. http://dx.doi.org/10.1109/JLT.2009.2022415.

Kamei, S., Shibata, T., Inoue, Y., 2009b. Compensation for second-order temperature dependence in athermal arrayed-waveguide grating realizing wide temperature range operation. IEEE Photonics Technol. Lett. 21, 1695–1697. http://dx.doi.org/10.1109/LPT.2009.2031819.

Leijtens, X.J.M., Kuhlow, B., Smit, M.K., 2006. Arrayed waveguide gratings. In: Wavelength Filters in Fibre Optics. Springer, pp. 125–187, Chapter 4.

Ma, J., et al., 2022. Broadened low anomalous dispersion in athermal aluminum nitride hybrid waveguides. IEEE Photonics J. 14, 1–7. http://dx.doi.org/10.1109/JPHOT.2022.3171435.

Pitris, S., Dabos, G., Mitsolidou, C., Alexoudi, T., Heyn, P. De, Campenhout, J. Van, Broeke, R., Kanellos, G.T., Pleros, N., 2018. Silicon photonic 8×8 cyclic arrayed waveguide grating router for o-band on-chip communication. Opt. Express 26, 6276–6284. http://dx.doi.org/10.1364/OE.26.006276.

Smit, M.K., van Dam, C., 1996. Phasar-based wdm-devices: Principles, design and applications. IEEE J. Sel. Top. Quantum Electron. 2, 236–250. http://dx.doi.org/10.1109/2944.577370.

Stoll, A., Zhang, Z., Haynes, R., Roth, M., 2017. High-resolution arrayed-waveguide-gratings in astronomy: Design and fabrication challenges. Photonics 4, 30. http://dx.doi.org/10.3390/photonics4020030.

Tang, X., Zheng, Y., Liu, J., Duan, J.-a., 2023. Optimization method for center frequency accuracy of high-channel-count arrayed waveguide grating in dense wavelength division multiplexing systems. Photonics 10, 1178. http://dx.doi.org/10.3390/photonics10111178.

Trenti, A., Borghi, M., Biasi, S., Ghulinyan, M., Ramiro-Manzano, F., Pucker, G., Pavesi, L., 2018. Thermo-optic coefficient and nonlinear refractive index of silicon oxynitride waveguides. AIP Adv. 8, 025311–1–025311–9.

Union, I.T., 2020. Spectral Grids for WDM Applications: DWDM Frequency Grid. Technical Report G.694.1, International Telecommunication Union, URL: https://www.itu.int/rec/T-REC-G.694.1-202010-I/en.

Wang, D., Jin, G., Yan, Y., Wu, M., 2001. Aberration theory of arrayed waveguide grating. J. Lightwave Technol. 19, 279–284. http://dx.doi.org/10.1109/50.917905.

van Wijk, A.C., Doerr, C.R., Akca, B.I., 2023. Custom arrayed waveguide gratings with improved performance. Adv. Photonics Res. http://dx.doi.org/10.1002/adpr.202300198.

van Wijk, A., Doerr, C.R., Ali, Z., Karabiyik, M., Akca, B.I., 2020. Compact ultrabroad-bandwidth cascaded arrayed waveguide gratings. Opt. Express 28, 14618–14626. http://dx.doi.org/10.1364/OE.394783.

Yang, C., Zhou, Z., Gao, X., Xu, Z., Han, S., Chong, Y., Min, R., Yue, Y., Duan, Z., 2024. Compact silicon-arrayed waveguide gratings with low nonuniformity. Sensors 24, 5303. http://dx.doi.org/10.3390/s24165303.

Yin, L., Lu, M., Wielunski, L., Song, W., Tan, J., Lu, Y., Jiang, W., 2012. Fabrication and characterization of compact silicon oxynitride waveguides on silicon chips. J. Opt. 14, 085501–1–085501–7.

Yuan, S., Feng, J., Yu, Z., Chen, J., Liu, H., Chen, Y., Guo, S., Huang, F., Akimoto, R., Zeng, H., 2023. Silicon nanowire-assisted high uniform arrayed waveguide grating. Nanomaterials 13, 182. http://dx.doi.org/10.3390/nano13010182.

Zhang, S., Gu, J., Yan, H., Xu, Z., Fan, Z., He, J.-J., 2025. Uniform low-loss cyclic arrayed waveguide grating router with input splitters and output combiners. Opt. Lett. 50, 5953–5956. http://dx.doi.org/10.1364/OL.573611.

Zhang, Y., Hsu, W.-L., Gatkine, P., Veilleux, S., Dagenais, M., 2023. High throughput arrayed waveguide grating with resolving power over 100,000. In: 2023 IEEE Photonics Conference. IPC, Orlando, FL, USA, pp. 1–2. http://dx.doi.org/10.1109/IPC57732.2023.10360795.